

Anisotropic x-ray magnetic linear dichroism at the $L_{2,3}$ edges of cubic Fe, Co, and Ni: *Ab initio* calculations and model theory

J. Kuneš^{1,2,*} and P. M. Oppeneer¹¹*Institute of Solid State and Materials Research, P.O. Box 270016, D-01171 Dresden, Germany*²*Institute of Physics, Academy of Sciences, Cukrovarnická 10, CZ-162 53 Prague, Czech Republic*

(Received 4 September 2002; published 30 January 2003)

We present an *ab initio* investigation of the x-ray magnetic linear dichroism (XMLD) in cubic Fe, Co, and Ni. We demonstrate that the XMLD spectra can be understood in terms of a simple model based on the energy derivatives of the $3d$ partial densities of states and the exchange splitting of the core levels, while the valence-band spin-orbit interaction plays only a marginal role for the overall shape of the spectra. Furthermore, our calculations predict the existence of a huge magnetocrystalline anisotropy of the XMLD spectra, which is of the same size as the XMLD spectrum itself. We provide a qualitative explanation of the anisotropy in terms of the above-mentioned model and suggest its experimental use for obtaining more information about the unoccupied d states.

DOI: 10.1103/PhysRevB.67.024431

PACS number(s): 75.30.Gw, 78.20.Ls

I. INTRODUCTION

X-ray magneto-optical spectroscopies have experienced a tremendous development during the last decade. Especially the x-ray magnetic circular dichroism (XMCD) has become established as a tool for the investigation of magnetic features on an element-resolved level (see, e.g., Refs. 1–4). A different x-ray spectroscopy, which was much less employed, is the x-ray magnetic linear dichroism (XMLD). The XMLD, which is of course measured with linearly polarized synchrotron radiation, is rooted in a microscopic origin quite distinct from that of the XMCD. Their distinction is apparent from the parity of the x-ray magneto-optical effect with respect to the magnetization \mathbf{M} : The XMCD signal is odd in \mathbf{M} (in lowest order linear in $\langle \mathbf{M} \rangle$) whereas the XMLD is even in \mathbf{M} (quadratic in lowest order). Although the XMLD is proportional to $\langle \mathbf{M}^2 \rangle$, it is a relatively small effect, accurate determination of which is far more difficult than that of the larger XMCD. Up to now only two XMLD spectra measured in transmission have been reported.^{5,6} The XMLD has also been measured in absorption, through the detection of secondary electrons for ferromagnetic^{7,8} and, in several cases, for antiferromagnetic films.^{9–12}

Only a few *ab initio* calculations of XMLD spectra were reported.^{6,7,13} Schwickert *et al.* (Ref. 7) obtained a fair agreement between measured and *ab initio* calculated XMLD spectra, in particular for the Fe L_3 edge. A very good agreement between the experimental and *ab initio* calculated x-ray Voigt rotation and ellipticity spectra of Co, which are directly proportional to the XMLD and the x-ray magnetic linear birefringence, respectively, was achieved by Mertins *et al.* (Ref. 6). A different approach was adopted by van der Laan who derived a proportionality between the integrated XMLD signal and the anisotropy of the spin-orbit interaction.¹⁴ In spite of the recent progress, it cannot be said that the XMLD is well understood.

In the present paper we report a detailed investigation of the XMLD at the $L_{2,3}$ edges of the cubic ferromagnets bcc Fe and fcc Co and Ni. First, we show that the XMLD spectrum

can be well approximated with a model in which the effect of the valence-band spin-orbit coupling is neglected and the exchange splitting of the $2p$ core states is considered to lowest nonvanishing order. The accuracy of the model is assessed by comparing spectra computed using the model with spectra obtained from precise *ab initio* calculations. The model formulates the XMLD spectrum as a sum of energy derivatives of the $3d$ partial densities of states scaled by the exchange splitting of the core levels, providing an intuitive understanding of the XMLD. In the case of spherical symmetry, the model relates the XMLD spectrum of ferromagnets to the energy derivative of their XMCD spectrum. Furthermore, we consider the magnetocrystalline anisotropy in the XMLD spectra, using both *ab initio* calculations and calculations based on the model. We predict a huge magnetocrystalline anisotropy to be present in the XMLD. In particular, this anisotropy is much larger than that observed previously in the XMCD of transition-metal multilayers.^{2,3} The origin of the huge magnetocrystalline anisotropy phenomenon is discussed and its implication for applied research is suggested.

II. FORMULATION OF THE XMLD

A. Macroscopic formulation

For the macroscopic formulation of the XMLD we resort to the classical theory of electromagnetic waves in a magnetic medium. For an in-plane magnetized film the XMLD is defined as the intensity difference of linearly polarized x rays transmitted with electric polarization \mathbf{E} parallel (T_{\parallel}) and perpendicular (T_{\perp}) to the magnetization. The x-ray synchrotron light is at normal incidence on the surface. In the material there are two eigenmodes with refractive indices n_{\perp} , n_{\parallel} , corresponding to $\mathbf{E} \perp \mathbf{M}$, $\mathbf{E} \parallel \mathbf{M}$, respectively. The XMLD asymmetry is given by^{6,15}

$$\begin{aligned} \text{XMLD} &= (T_{\parallel} - T_{\perp}) / (T_{\parallel} + T_{\perp}) \approx \frac{\omega d}{c} \text{Im}[n_{\parallel} - n_{\perp}] \\ &\approx \frac{\omega d}{2cn} \text{Im} \left[\epsilon_{\parallel} - \epsilon_{\perp} - \frac{\epsilon_{od}^2}{\epsilon_{\perp}} \right]. \end{aligned} \quad (1)$$

Here d is the thickness of the film, ω the frequency of the light, ϵ_{\parallel} and ϵ_{\perp} , are the diagonal components of the dielectric tensor for orientation of E parallel and normal, respectively, to the magnetization, \bar{n} is the average refractive index, and ϵ_{od} is the off-diagonal component of the dielectric tensor. The latter component is present for a ferromagnetic material and gives, in the x-ray regime, rise to the XMCD or the x-ray Faraday effect.^{16–18} It was previously shown that $\epsilon_{od}^2/\epsilon_{\perp}$ is about a 100 times smaller than $\epsilon_{\parallel} - \epsilon_{\perp}$ at the L edges of ferromagnetic transition metals.⁶ Consequently, we can ignore this contribution to the XMLD. Since at the edge the energy variation is negligible as well, we shall in the following discuss the $\text{Im}[\epsilon_{\parallel} - \epsilon_{\perp}]$ spectrum, which we shall name “XMLD” as well. An abbreviation that we use in the following for the absorptive part of ϵ is $\text{Im } \epsilon \equiv \epsilon^{(2)}$.

B. Exchange splitting of the core states

Our intention is to pursue both a relativistic *ab initio* calculation of the XMLD spectra, as well as a model description of the spectra obtained under physically motivated approximations. In both approaches, we start from the initial $2p$ states that can be—in a very good approximation—described by an atomic calculation in the spherical part of the crystal potential. The dominant interaction determining the spin-angular character of the wave function is the spin-orbit coupling, which splits the $2p$ level into the $2p_{1/2}$ and $2p_{3/2}$ doublets. The spin-orbit splitting is larger than 10 eV in Fe, Co, and Ni. On top of this the exchange field caused by the spin-polarized valence electrons (spin-only interaction) splits the $2p_{1/2}$ and $2p_{3/2}$ levels further. The following treatment of the $2p$ states is adopted in the present work. The radial parts of the $2p$ functions are calculated using the radial Dirac equation in the spin-averaged spherical part of the crystal potential. The spherical part of the exchange field is then accounted for using first-order perturbation theory. This means that the energies are renormalized, and the wave functions are classified by j, j_z quantum numbers; i.e., the mixing of $2p_{1/2}$ and $2p_{3/2}$ characters is neglected. This approximation is justified by the size of the exchange splitting being below 1 eV. The resulting spectrum of the exchange-split $2p$ states consists of a $2p_{1/2}$ doublet and a $2p_{3/2}$ quadruplet with an equidistant splitting Δ_j . The energy increases with j_z for the $2p_{1/2}$ levels and decreases with j_z for the $2p_{3/2}$ levels (+1 is assumed to be the majority spin projection). Δ_j is computed from

$$\Delta_j = \frac{2}{3} \int r^2 R_j^2(r) b(r) dr, \quad (2)$$

where $R_j(r)$ is the respective radial part of the wave function and $b(r)$ the exchange field. The Δ_j for $j=1/2$ and $j=3/2$ differ by a few percent, and therefore this difference is neglected in the model calculations.

We have dwelled upon the exchange splitting of the $2p$ core states, because only once this quantity is included a XMLD of reasonable size can be obtained.⁶ The exchange splitting of the $2p$ states is thus a prerequisite to describe properly the XMLD. Its role for the XMCD was studied

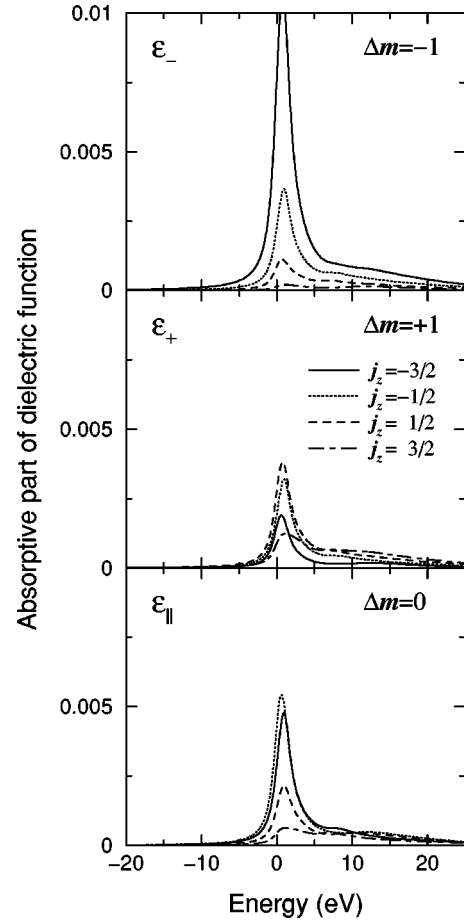


FIG. 1. Decomposition of the absorptive part of the dielectric functions $\epsilon_{\perp}^{(2)}$, $\epsilon_{+}^{(2)}$, and $\epsilon_{\parallel}^{(2)}$ with regard to the four exchange-split $2p_{3/2}$ core states, computed for fcc Co. The XMLD spectrum is proportional to $\epsilon_{\parallel}^{(2)} - \frac{1}{2}(\epsilon_{+}^{(2)} - \epsilon_{-}^{(2)})$ and would practically vanish if the small energy shifts in the individual j_z peaks were not present.

previously.^{19,20} A first understanding of the origin of the XMLD can be gained from considering a decomposition of the dielectric functions with regard to the exchange split j_z states. To this end a reformulation of ϵ_{\perp} is practical. For a uniaxial ferromagnetic material one can write $\epsilon_{\perp} = \frac{1}{2}(\epsilon_{+} + \epsilon_{-})$, with $\epsilon_{\pm} = \epsilon_{\perp} \pm i\epsilon_{od}$. The XMLD spectrum is thus proportional to $\epsilon_{\parallel} - \frac{1}{2}(\epsilon_{+} + \epsilon_{-})$, whereas the XMCD spectrum is proportional to $\epsilon_{+} - \epsilon_{-}$ (more precisely, it is $(\omega d/2c\bar{n})[\epsilon_{+}^{(2)} - \epsilon_{-}^{(2)}]$). The optical transition matrix elements obey the dipolar selection rules on the angular momentum quantum numbers l, m , of the initial and final states such that $\Delta m = \pm 1$ or $\Delta m = 0$ and $\Delta l = \pm 1$. To ϵ_{\perp} only transitions with $\Delta m = \pm 1$ contribute, whereas to ϵ_{\parallel} only $\Delta m = 0$ transitions contribute. The XMLD is thus the intensity difference between the resonant transitions with $\Delta m = 0$ and the averaged $\Delta m = \pm 1$ transitions, whereas the XMCD relates to the difference between the $\Delta m = +1$ and $\Delta m = -1$ transitions. An illustration of the decomposed dielectric functions at the L_3 edge of fcc Co is given in Fig. 1. Shown are the separate contributions of the initial exchange-split $j_z = -3/2, -1/2, 1/2,$ and $3/2$ levels to the absorptive part of the permittivities, $\epsilon_{\perp}^{(2)}$, $\epsilon_{+}^{(2)}$, and $\epsilon_{\parallel}^{(2)}$, respectively. The

rather small energy shifts ($\Delta \approx 260$ meV for fcc Co) in the individual spectra give, when the spectra are summed, rise to the XMLD. The computational method that we applied to compute the permittivities was outlined in Ref. 21. Details of the calculations are mentioned below.

III. MODEL FOR XMLD IN CUBIC SYSTEMS

The overall structure of x-ray absorption and XMCD spectra in 3d metals can be well described using the nonrelativistic d partial densities of states; i.e., spin-orbit coupling is not considered for the valence states. The spin-orbit coupling constant ξ of the 3d ferromagnets is about 80–100 meV, which is smaller than Δ . For example, Δ is about 320 meV for Fe. However, for Ni, Δ is only 100 meV, which already indicates that the neglect of the valence-band spin-orbit coupling could be a poor approximation. A comparison to *ab initio* calculated spectra shall provide the test of the validity of the approximation. The valence-band spin-orbit coupling leads to a modification of the x-ray absorption spectrum (XAS) branching ratio and the asymmetry of XMCD peaks, effects which become apparent by integration of the spectra over both edges. Recently we presented a calculation of the x-ray Voigt effect⁶ (related to the XMLD) at the L_3 edge of Co. As a result of this calculation it became clear that a major part of the XMLD can be captured without considering the valence-band spin-orbit coupling.

In the following we present model calculations of the XAS, XMCD, and XMLD in the cubic 3d ferromagnets. The model uses only the d partial densities of states and the size of the $2p$ exchange splitting as an input. We compare the model calculations to what we call the “full” calculations, implementation of which is described in detail in Ref. 21. The full calculation takes into account the valence-band spin-orbit coupling, $2p \rightarrow 4s$ transitions, as well as the energy dependence of the radial matrix elements, and the lowering of the crystal symmetry due to the spin-orbit coupling. Both the model and the full calculations use the dipolar approximation to the transition matrix elements and neglect core-hole effects.

When $p \rightarrow s$ transitions are neglected and the radial part of the transition matrix element is assumed to be the same for all transitions, the expression for the absorptive part of the permittivity reduces to

$$\epsilon_{\mu}^{(2)}(\omega) \propto \sum_{m,s} a_{\gamma s}^{\mu}(j) f_{ms} \left(\omega \pm \frac{\gamma}{2} \Delta \right), \quad (3)$$

with $\gamma/2 \equiv m - \mu + s$, and $\mu = +1, -1$, or 0 (note that $\epsilon_0 \equiv \epsilon_{\parallel}$). The $f_{ms}(\omega)$ stand for the d partial densities of unoccupied states indexed with orbital moment projection m and spin projection s , and $a_{\gamma s}^{\mu}(j)$ denotes the angular part of the transition probability for a transition from the $2p_{j\gamma/2}$ state to the $3d_{ms}$ state (m is determined by the dipolar selection rule). The shift of the contributions of different core levels results from the exchange splitting of the core levels. The plus sign applies to the L_2 edge and the minus sign to the L_3 edge. The $a_{\gamma s}^{\mu}(j)$ are merely numerical constants, defined by

$$a_{\gamma s}^{\mu}(j) = \left| \left(1(m - \mu) \frac{1}{2} s \left| j \frac{\gamma}{2} \right\rangle \langle Y_{2m} | Y_{1\mu} | Y_{1m - \mu} \right) \right|^2, \quad (4)$$

where the Y_{lm} are the spherical harmonics, and the projection coefficients of the relativistic wave functions on the $|ls\rangle$ basis (Clebsch-Gordan coefficients) are denoted by the parentheses. The numerical values for the $a_{\gamma s}^{\mu}(j)$ coefficients are listed in Tables II and III in Appendix B. For sake of simplicity we use further on the \uparrow, \downarrow notation for $s = +\frac{1}{2}, -\frac{1}{2}$, and we drop the j index from $a_{\gamma s}^{\mu}(j)$ since the two edges are treated independently and so it is clear which value of j is considered. The contribution of the product of the matrix elements for opposite spin channels is neglected in Eq. (3). This is consistent with neglecting the valence-band spin-orbit coupling; however, this omission is well justified in 3d system even if the valence-band spin-orbit coupling is taken into account.

An important remark regarding Eq. (3) concerns the choice of the quantization axis, with respect to which the d partial densities are expressed. Equation (3) applies to the quantization axis collinear to the magnetization vector. Any magnetocrystalline anisotropy of the XMLD occurring within the model therefore arises from the change of the quantization axis.

Next, we evaluate Eq. (3) to obtain the XAS, XMCD, and XMLD spectra. Furthermore, the magnetocrystalline anisotropy of the XMLD is investigated by calculating the XMLD for both the (001) and (111) orientations of the magnetization. We need for the evaluation of Eq. (3) relations for the partial densities of state $f_{ms}(\omega)$, which are discussed in Appendix A. Due to the neglect of the spin-orbit coupling in the final states, time-reversal symmetry holds for these, as the hybridization between the core and valence states is negligible, too. As a consequence, we have $f_{-ms}(\omega) = f_{ms}(\omega)$. A second relation, which can be seen to follow from Table I in Appendix A, is

$$f_{2s}(\omega) = \frac{1}{2} [f_{0s}(\omega) + f_{1s}(\omega)], \quad (5)$$

which holds for both the (001) and (111) quantization axes. The number of independent partial densities of states is reduced thereby to two per spin channel.

We start with the derivation for the L_2 edge. From Eq. (3) we find

$$\begin{aligned} \epsilon_{+}^{(2)}(\omega) &= a_{-1\uparrow}^{+} f_{0\uparrow}(\omega) + a_{-1\downarrow}^{+} f_{1\downarrow}(\omega) \\ &\quad + a_{1\uparrow}^{+} f_{1\uparrow}(\omega + \Delta) + a_{1\downarrow}^{+} f_{2\downarrow}(\omega + \Delta), \end{aligned} \quad (6)$$

$$\begin{aligned} \epsilon_{-}^{(2)}(\omega) &= a_{-1\uparrow}^{-} f_{-2\uparrow}(\omega) + a_{-1\downarrow}^{-} f_{-1\downarrow}(\omega) \\ &\quad + a_{1\uparrow}^{-} f_{-1\uparrow}(\omega + \Delta) + a_{1\downarrow}^{-} f_{0\downarrow}(\omega + \Delta), \end{aligned} \quad (7)$$

$$\begin{aligned} \epsilon_{\parallel}^{(2)}(\omega) &= a_{-1\uparrow}^0 f_{-1\uparrow}(\omega) + a_{-1\downarrow}^0 f_{0\downarrow}(\omega) \\ &\quad + a_{1\uparrow}^0 f_{0\uparrow}(\omega + \Delta) + a_{1\downarrow}^0 f_{1\downarrow}(\omega + \Delta). \end{aligned} \quad (8)$$

Note that for convenience we chose the energy zero at the $j_z = -\frac{1}{2}$ level. The Δ -shifted functions are Taylor expanded and the lowest order term in Δ is retained, while we denote

the derivate of f_{ms} with respect to the energy by f'_{ms} . Furthermore, we apply the relation $f_{2s} = \frac{1}{2}(f_{0s} + f_{1s})$, and we insert the numerical values for $a_{\gamma s}^{\mu}$. For the XAS the averaged diagonal permittivity $\bar{\epsilon} \equiv \frac{1}{3}(2\epsilon_{\perp} + \epsilon_{\parallel})$ is given by

$$\begin{aligned} \bar{\epsilon}^{(2)}(\omega) &\propto 6[f_{1\uparrow}(\omega) + f_{1\downarrow}(\omega)] + 4[f_{0\uparrow}(\omega) + f_{0\downarrow}(\omega)] \\ &= 2 \text{Tr}(D_{\uparrow} + D_{\downarrow}), \end{aligned} \quad (9)$$

where D_{\uparrow} and D_{\downarrow} are the unoccupied d density matrices for spin up and spin down, respectively. The d partial densities of state are the diagonal elements of the density matrices, and $\text{Tr}(D_{\uparrow, \downarrow})$ is the total d -spin density. For the XMCD we obtain

$$\begin{aligned} \epsilon_{+}^{(2)}(\omega) - \epsilon_{-}^{(2)}(\omega) &\propto -6[f_{1\uparrow}(\omega) - f_{1\downarrow}(\omega)] - 4[f_{0\uparrow}(\omega) - f_{0\downarrow}(\omega)] \\ &= -2 \text{Tr}(D_{\uparrow} - D_{\downarrow}). \end{aligned} \quad (10)$$

Likewise, for the XMLD we obtain

$$\begin{aligned} \epsilon_{\parallel}^{(2)}(\omega) - \epsilon_{\perp}^{(2)}(\omega) &\propto \Delta \{4[f'_{0\uparrow}(\omega) - f'_{0\downarrow}(\omega)] - 3[f'_{1\uparrow}(\omega) \\ &\quad - f'_{1\downarrow}(\omega)]\}. \end{aligned} \quad (11)$$

Following the same procedure for the L_3 edge we arrive at (relative to the $j_z = -\frac{3}{2}$ level)

$$\begin{aligned} \epsilon_{+}^{(2)}(\omega) &= a_{-3\downarrow}^{+} f_{0\downarrow}(\omega) + a_{-1\uparrow}^{+} f_{0\uparrow}(\omega - \Delta) \\ &\quad + a_{-1\downarrow}^{+} f_{1\downarrow}(\omega - \Delta) a_{1\uparrow}^{+} f_{1\uparrow}(\omega - 2\Delta) \\ &\quad + a_{1\downarrow}^{+} f_{2\downarrow}(\omega - 2\Delta) a_{3\uparrow}^{+} f_{2\uparrow}(\omega - 3\Delta), \end{aligned} \quad (12)$$

$$\begin{aligned} \epsilon_{-}^{(2)}(\omega) &= a_{-3\downarrow}^{-} f_{-2\downarrow}(\omega) + a_{-1\uparrow}^{-} f_{-2\uparrow}(\omega - \Delta) \\ &\quad + a_{-1\downarrow}^{-} f_{-1\downarrow}(\omega - \Delta) a_{1\uparrow}^{-} f_{-1\uparrow}(\omega - 2\Delta) \\ &\quad + a_{1\downarrow}^{-} f_{0\downarrow}(\omega - 2\Delta) a_{3\uparrow}^{-} f_{0\uparrow}(\omega - 3\Delta), \end{aligned} \quad (13)$$

$$\begin{aligned} \epsilon_{0}^{(2)}(\omega) &= a_{-3\downarrow}^0 f_{-1\downarrow}(\omega) + a_{-1\uparrow}^0 f_{-1\uparrow}(\omega + \Delta) \\ &\quad + a_{-1\downarrow}^0 f_{0\downarrow}(\omega - \Delta) a_{1\uparrow}^0 f_{0\uparrow}(\omega - 2\Delta) \\ &\quad + a_{1\downarrow}^0 f_{1\downarrow}(\omega - 2\Delta) a_{3\uparrow}^0 f_{1\uparrow}(\omega - 3\Delta). \end{aligned} \quad (14)$$

The quantities corresponding to the XAS, XMCD, and XMLD at the L_3 edge become, respectively,

$$\begin{aligned} \bar{\epsilon}^{(2)}(\omega) &\propto 12[f_{1\uparrow}(\omega) + f_{1\downarrow}(\omega)] + 8[f_{0\uparrow}(\omega) + f_{0\downarrow}(\omega)] \\ &= 4 \text{Tr}(D_{\uparrow} + D_{\downarrow}), \end{aligned} \quad (15)$$

$$\begin{aligned} \epsilon_{+}^{(2)}(\omega) - \epsilon_{-}^{(2)}(\omega) &\propto 6[f_{1\uparrow}(\omega) - f_{1\downarrow}(\omega)] + 4[f_{0\uparrow}(\omega) - f_{0\downarrow}(\omega)] \\ &= 2 \text{Tr}(D_{\uparrow} - D_{\downarrow}), \end{aligned} \quad (16)$$

$$\begin{aligned} \epsilon_{\parallel}^{(2)}(\omega) - \epsilon_{\perp}^{(2)}(\omega) &\propto \Delta \{4[f'_{0\uparrow}(\omega) - f'_{0\downarrow}(\omega)] - 3[f'_{1\uparrow}(\omega) - f'_{1\downarrow}(\omega)]\}. \end{aligned} \quad (17)$$

Although a calculation of the XAS and XMCD is not the primary aim of this work, we point out that the model does provides the commonly expected results for these. The XAS branching ratio $I_{L_3}/(I_{L_2} + I_{L_3})$ is 2/3, and the integrated L_2 and L_3 XMCD peaks are equal and have opposite sign. The XMCD orbital-moment sum rule²² would thus give zero, consistent with the neglect of the spin-orbit interaction in the valence states. The integrated L_2 and L_3 XMCD peaks can be written as the difference of the integrated occupied spin densities of spin up and spin down, i.e., the spin moment, which is consistent with the spin-moment sum rule.²³ (The $\langle T_z \rangle$ term which also occurs in the spin-moment sum rule can be omitted for cubic $3d$ materials.²⁴) We note, furthermore, that the model expressions for the XAS, XMCD, and XMLD obey the known parity relations with respect to magnetization reversal. The XAS is invariant under magnetization reversal, while XMCD is odd, and the XMLD is even under $\mathbf{M} \rightarrow -\mathbf{M}$, as both Δ and $f'_{m\uparrow} - f'_{m\downarrow}$ change sign. Under the present approximations there is, to lowest order in Δ , no magnetocrystalline anisotropy of the XAS and XMCD, because these quantities are proportional to combinations of the traces of the density matrices. These traces are invariant under rotations of the quantization axis; see Appendix A. This is not the case for the XMLD, since its expression contains separate elements of the d partial density of states.

Our central result concerns the XMLD expressions, which main features can be summarized as follows. The same spectral dependence, being proportional to the product of Δ and the linear combination of the derivatives of the partial densities of state, is expected for both the L_2 and L_3 edges. A nonzero magnetocrystalline anisotropy can occur to first order in Δ . Using the results for the partial densities collected in Table I, we can reexpress the XMLD for the (001) and (111) magnetization orientations in terms of the two independent elements A and B of the density matrix. These elements are related to the e_g and t_{2g} spin densities of state such that the total e_g spin density of states is $2B$, and the total t_{2g} spin density of states is $3A$ (see Appendix A). The XMLD at both the L_2 and L_3 edges is, for a (001) magnetization, proportional to

$$\begin{aligned} \epsilon_{\parallel}^{(2)}(\omega) - \epsilon_{\perp}^{(2)}(\omega)|_{(001)} &\propto \Delta = \{3[A'_{\uparrow}(\omega) - A'_{\downarrow}(\omega)] + 4[B'_{\uparrow}(\omega) - B'_{\downarrow}(\omega)]\}, \end{aligned} \quad (18)$$

whereas for the (111) magnetization the XMLD becomes

$$\begin{aligned} \epsilon_{\parallel}^{(2)}(\omega) - \epsilon_{\perp}^{(2)}(\omega)|_{(111)} &\propto \Delta \{3[A'_{\uparrow}(\omega) - A'_{\downarrow}(\omega)] - 2[B'_{\uparrow}(\omega) - B'_{\downarrow}(\omega)]\}. \end{aligned} \quad (19)$$

For a cubic material a definite magnetocrystalline anisotropy in the XMLD is thus predicted, the magnitude of which is addressed later on.

The above (001) and (111) XMLD expressions become equal when we adopt spherical symmetry, for which all m -projected partial densities f_{ms} are equal and thus $A \equiv B$. Substituting the numerical constants, the XMCD for spherical symmetry can be written as $\epsilon_+^{(2)} - \epsilon_-^{(2)} \approx \pm 0.05305(f_{\uparrow} - f_{\downarrow})$, where the plus sign holds for the L_3 and the minus sign for the L_2 edge, and $f_{ms} \equiv f_s$. Similarly, the XMLD is given by $\epsilon_{\parallel}^{(2)} - \epsilon_{\perp}^{(2)} \approx -0.00531\Delta(f'_{\uparrow} - f'_{\downarrow})$. Combining these two equations leads to

$$\epsilon_{\parallel}^{(2)}(\omega) - \epsilon_{\perp}^{(2)}(\omega) \approx \mp 0.1\Delta[\epsilon_+^{(2)}(\omega) - \epsilon_-^{(2)}(\omega)]'. \quad (20)$$

For spherical symmetry the XMLD is thus proportional to the derivative of the XMCD spectrum. Although only a few XMLD spectra were reported⁵⁻⁷ for 3d transition metals, the shape of the measured spectra is consistent with Eq. (20). The XMLD spectrum is zero directly at the L_3 edge, where the XMCD maximum occurs. Before and after the edge the XMLD spectrum displays lobes with opposite sign, in agreement with the negative or positive derivative of the XMCD spectrum before or after, respectively, the edge.^{5,6}

IV. NUMERICAL RESULTS

In the following we shall compare the spectra calculated with the model to spectra obtained from full calculations. The electronic structure calculations were performed using the full-potential linearized augmented-plane-wave code WIEN97 (Ref. 25). First, without spin-orbit coupling the electronic structure was converged within the cubic symmetry and the respective partial densities of states were calculated for the model calculations. Subsequently, the spin-orbit coupling was added²⁶ using the second variation approach with the magnetization confined either to the (001) or (111) direction and the calculation was converged to self-consistency. All calculations were performed on k meshes of more than 500 k points in the irreducible part of the Brillouin zone. In the case of Ni, test calculations were performed on up to 2500 k points in 1/16th of the fcc Brillouin zone, which gave the same results. To obtain smooth spectra Lorentzian broadening with broadening parameters 0.7–0.8 eV and 1.2–1.3 eV for the L_3 and L_2 edges, respectively, was performed on the spectra of the full calculations, and a similar broadening was applied on the partial densities of states in the model calculations.

Results for the calculated XAS, XMCD, and XMLD spectra are presented in Figs. 2, 3, and 4, for (001) bcc Fe, fcc Co, and fcc Ni, respectively. Symbols show the spectra obtained by the full calculation, while the lines show those of the model calculation. The spectra are normalized to yield the height of the L_3 XAS peak equal to 1. The mismatch between the full calculation and the model calculation for the L_2 XAS peak arises from the fact that in the full calculation the tail of the L_3 peak adds up to the intensity of the L_2 peak, while in the model the two peaks are calculated independently. No such mismatch occurs for the XMCD and XMLD

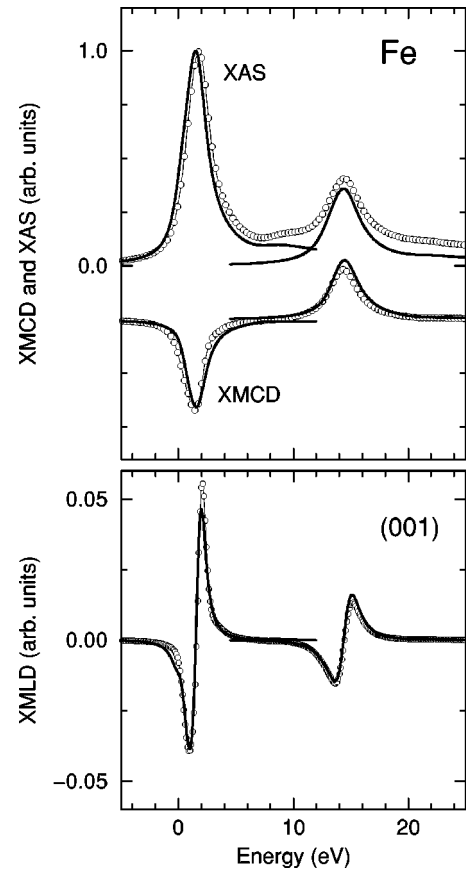


FIG. 2. The XAS, XMCD, and XMLD spectra of (001) bcc Fe as obtained from the model calculation (solid curves) and the full calculation (symbols). The XAS spectrum at the L_3 edge has been normalized to 1.

spectra because the individual L_3 and L_2 spectra are zero outside the immediate vicinity of the edge. Comparing the full and model calculations for the three quantities we observe the following: Apart from the understandable L_2 mismatch, the full and model calculations yield XAS spectra in good agreement. Also for the XMCD the full and model spectra agree. The effect of the valence-band spin-orbit coupling can be well recognized. It causes a small enhancement of the L_3 peak and a small reduction of the L_2 peak. Thereby it leads to a transfer of some spectral weight from the L_2 edge to the L_3 edge, which is experimentally well known (e.g., Refs. 1–4) and consistent with the orbital-momentum sum rule.²²

Considering next the XMLD spectra, we observe a good agreement between the full and model calculations for Fe and Co, but for Ni the agreement is unsatisfactory (see Fig. 7). For each material the spectra at the L_2 edge match slightly better than the spectra at the L_3 edge. This is connected to the accuracy of the Taylor expansion. An obvious assumption when replacing the shifted functions by their first-order Taylor expansion is that the variation of the function on the scale of the shift is small. This condition is better fulfilled at the L_2 edge than at the L_3 edge, because, first, the total shift is smaller (only Δ at the L_2 compared to a total shift 3Δ at the L_3 edge), and second, the L_2 peaks are typi-

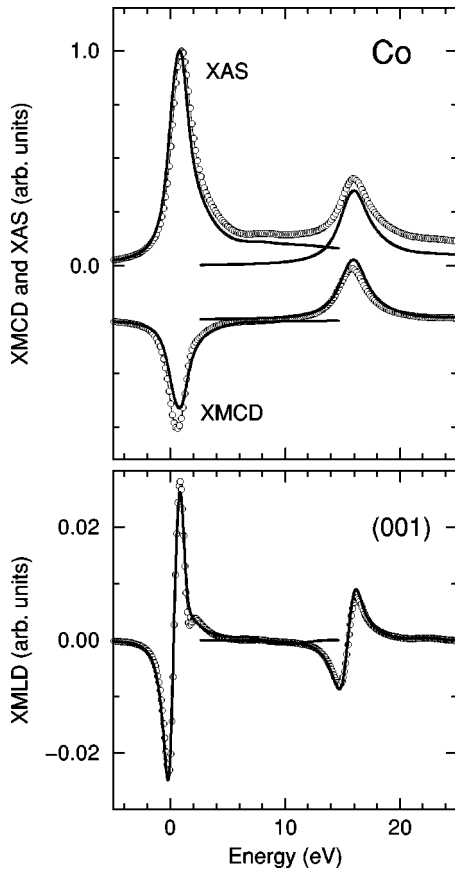


FIG. 3. As in Fig. 2, but for (001) fcc Co.

cally broader due to lifetime effects. The effect of the valence-band spin-orbit coupling is best seen at the positive peaks in both Fe and Co. While the model is below the full calculation at the L_3 edge, it is above the full calculation at the L_2 edge. The magnitudes of the XMLD peaks vary markedly. The L_3 XMLD peak of Co is about half as large as that of Fe, but for Ni the L_3 peak is about 10 times smaller than that of Fe. The different exchange splittings of the core and valence states are responsible for these different XMLD magnitudes. The scaling of the XMLD peaks follows roughly that of M_s^2 , the square of the spin moment, the ratios of which are 0.5 for Co/Fe and 0.08 for Ni/Fe. The model calculation fails to reproduce the full calculation for Ni. The reason for this failure is the neglect of the valence-band spin-orbit coupling, which becomes important for the small size of the XMLD in Ni. To investigate the contribution of the valence-band spin-orbit coupling, we computed the XMLD spectrum including this effect, but neglecting the exchange splitting of the core states. The resulting spectrum is shown in Fig. 4 by the dashed curve. The XMLD contribution stemming from spin-orbit coupling in the valence states is obviously not negligible, and adding it to the XMLD of the model calculation would reproduce reasonably the XMLD of the full calculation.

A second part of our investigations is aimed at the magnetocrystalline anisotropy in the XMLD spectrum. The XMLD spectra were computed for the (001) and (111) magnetization orientations using both the model and the full ap-

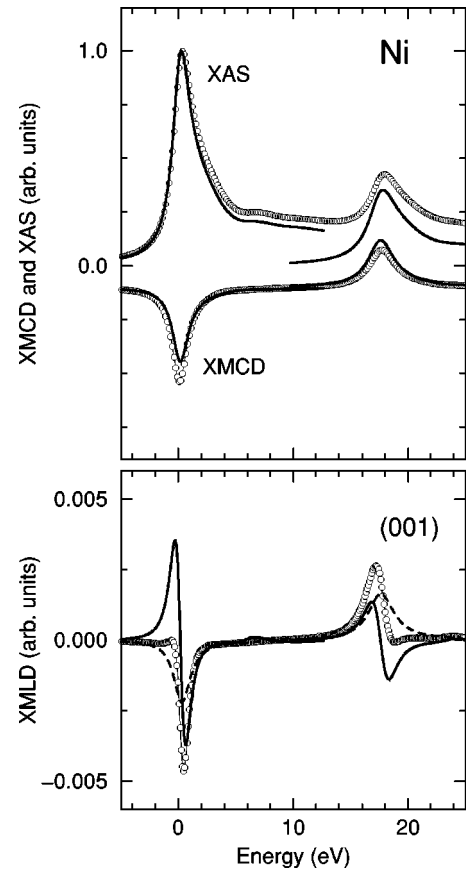


FIG. 4. As in Fig. 2, but for (001) fcc Ni. The dashed curve in the bottom panel shows the XMLD spectrum calculated without the $2p$ core exchange splitting, but including the valence-band spin-orbit coupling.

proach. The results are shown in Figs. 5, 6, and 7, for Fe, Co, and Ni. The degree of agreement between the model (solid curves) and the full spectra (symbols) for the (111) magnetization is similar to, or even better, than that discussed above for the (001) case. Note that we have scaled the XMLD spectra in Figs. 5–7 by normalizing the L_3 XAS peak height to 100 instead of to 1. In all three investigated systems the magnetocrystalline anisotropy predicted for the XMLD spectra is huge: it is of the same size as the XMLD spectrum itself. The anisotropy reflects directly the deviation of the m -dependent partial densities of states in the cubic symmetry from the spherically symmetric case ($A=B$), where the anisotropy would vanish. These partial densities of state are the quantities that are decisive for many magnetic properties of the $3d$ ferromagnets, such as, for example, the orbital moment. Their determination would become possible by accurate XMLD measurements. The XMLD spectra for the two magnetization directions vary, moreover, quite distinctly with the $3d$ material. For example, at the L_2 edge the Fe (111) XMLD spectrum is opposite in shape to that of Ni (111). The (111) spectra for Fe and Ni display a double-lobe structure, but for Co the (111) L_2 and L_3 spectra display a triple-lobe structure. The (001) spectra of bcc Fe and fcc Co are, on the other hand, rather similar. For Ni we have investigated the importance of the valence-band spin-orbit cou-

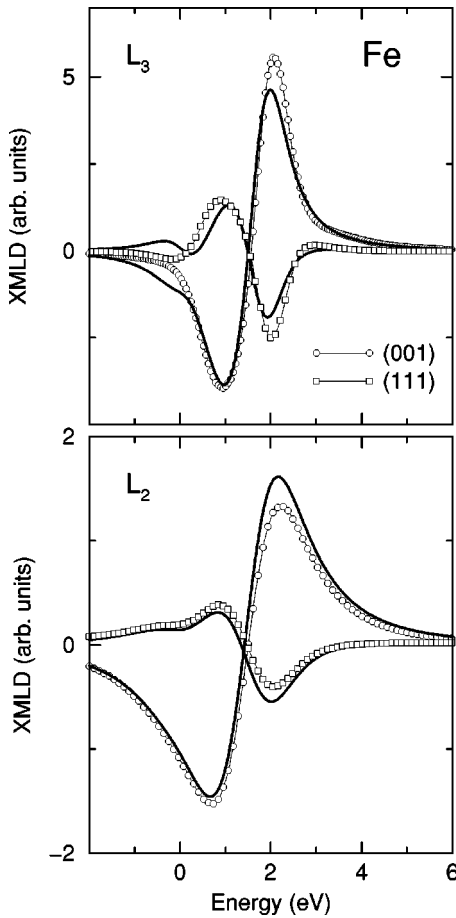


FIG. 5. The calculated XMLD spectra of (001) and (111) bcc Fe, for the L_3 edge (top) and the L_2 edge (bottom). The symbols show the results of the full *ab initio* calculations, whereas the solid curves show the spectra obtained by the model calculations. The spectra are normalized by scaling the L_3 XAS peak to 100.

pling also for the (111) magnetization. The XMLD spectra that were computed without the $2p$ exchange splitting, but with the valence-band spin-orbit coupling, are shown by the dashed curves with the small symbols in Fig. 7. Surprisingly, a better matching between the model and full calculations is found for the (111) magnetization direction as compared to the (001) direction. The contribution of the valence-band spin-orbit coupling is different for the two orientations. This likely corresponds to changes in the partial density of states that are specific for Ni. A detailed explanation of this behavior is, however, outside the scope of this paper.

V. CONCLUSIONS

The success of the model calculations in describing the XMLD as compared to the full calculations leads us to draw the following conclusions. The XMLD spectra can basically be understood in terms of the $2p$ core-state exchange splitting and the derivatives of the d partial densities of states. Unlike the XAS and XMCD, which come out to be isotropic (with regard to the orientation of the magnetization to the crystallographic axes), the XMLD is predicted to exhibit a pronounced magnetocrystalline anisotropy. This is a conse-

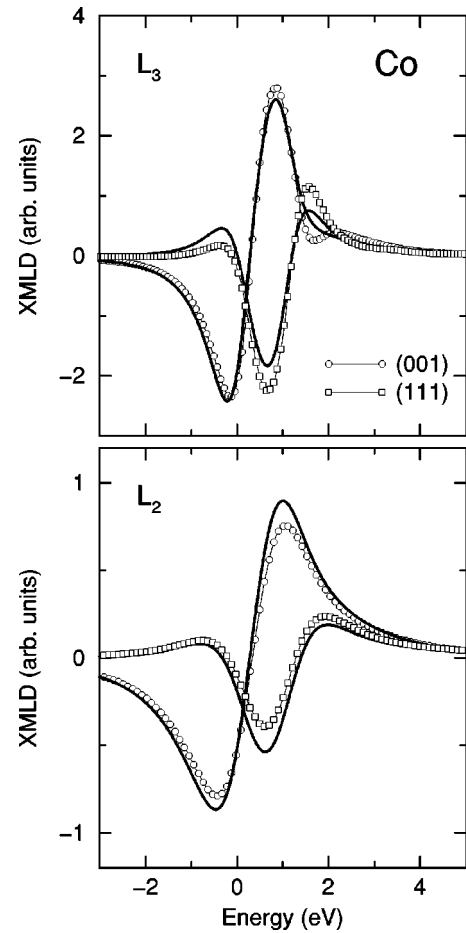


FIG. 6. As in Fig. 5, but for (001) and (111) fcc Co.

quence of the fact that the XAS and XMCD are proportional to the traces of the d density matrices, while the XMLD is proportional to a combination of individual partial densities of states, which is not invariant upon the change of the quantization axis. Consequently, the XMLD anisotropy exists already when the valence-band spin-orbit coupling is neglected.

The present model is obviously not able to capture the XMLD sum rule,¹⁴ which states that $I_{L_3,\parallel} - I_{L_3,\perp} - 2(I_{L_2,\parallel} - I_{L_2,\perp})$ is proportional to the anisotropy of the spin-orbit interaction $\langle I \cdot s \rangle$. As no valence-band spin-orbit coupling is present in the model the integrated XMLD intensity per edge is exactly zero. We note, furthermore, that the XMLD sum rule and our model adopt different points of view. While the sum rule, arising from the completeness of the initial states, provides information about the anisotropy of the spin-orbit interaction in the final states, it does not deal with the spectral shape of the XMLD. It was derived adopting spherical symmetry and the exchange splitting of the core states was neglected. Conversely, the presented model cannot capture the anisotropy of the spin-orbit interaction, but provides a simple semiquantitative description of the shape of the XMLD spectra. The full calculations suggest that the valence-band relativistic effects have, except for Ni, only a marginal impact on the XMLD spectra. Therefore, to extract integrated quantities precise cancellations of large numbers

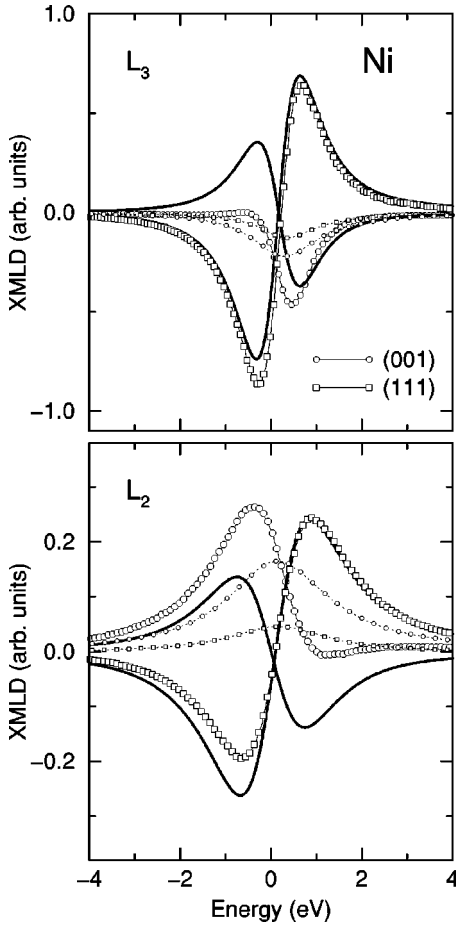


FIG. 7. As in Fig. 5, but for (001) and (111) fcc Ni. The dashed curves with the small symbols show the XMLD spectra computed without the core exchange splitting, but with the valence-band spin-orbit coupling included.

are required, which is a possible obstacle already in the calculations, and it might diminish the prospects of an efficient experimental use of the XMLD sum rule.

Besides providing a simple understanding of the measured shape of the XMLD spectra, the presented model suggests a prescription for obtaining all the elements of the difference between majority and minority spin density matrices. By measuring the XMLD for two different magnetization orientations, the spin-polarized part of the e_g and t_{2g} unoccupied partial densities of states could be determined for the cubic $3d$ ferromagnets. Last, although it is still relatively difficult to measure the XMLD, the magnetocrystalline anisotropy that we predict for the XMLD of bcc Fe and fcc Co and Ni should be large enough to be observed in experiments on single-crystalline films. Such experiments are highly desirable, as these would put to an arduous test the predicted anisotropic XMLD spectra.

ACKNOWLEDGMENTS

We thank Hans-Christoph Mertins and Claus Schneider for valuable discussions. This work was supported financially by Grant No. A1010214 of the Academy of Sciences of the Czech Republic.

APPENDIX A: d OCCUPATION MATRIX IN CUBIC SYMMETRY

The spin- and m -projected d partial densities of states are the appropriate quantities for discussing the absorption at the $L_{2,3}$ edges. While the information contained in the individual partial densities of states depends on the choice of the quantization axis, the full density matrix provides a generalization of the partial densities (which are its diagonal elements), which is independent of the quantization axis. Here we discuss the form of the d density matrix for a cubic system without spin-orbit coupling. We point out that even if the local symmetry of a particular atomic site is lower than cubic, the cubic symmetry is restored upon summing over equivalent positions, which is the relevant quantity for x-ray spectroscopy.

If the spin-orbit coupling is not considered, the d density matrix $D_{m,m',s,s'}$ can be decomposed into two independent spin blocks. To start with, when the quantization axis is chosen along a fourfold axis, each of the spin blocks $D_{mm'}$ possesses the following form with only two real independent elements, denoted A and B :

$$D = \begin{pmatrix} \frac{B+A}{2} & 0 & 0 & 0 & \frac{B-A}{2} \\ 0 & A & 0 & 0 & 0 \\ 0 & 0 & B & 0 & 0 \\ 0 & 0 & 0 & A & 0 \\ \frac{B-A}{2} & 0 & 0 & 0 & \frac{B+A}{2} \end{pmatrix}. \quad (\text{A1})$$

This form is easy to understand. The fourfold symmetry about the quantization axis allows only those $D_{mm'}$ elements to be nonzero for which $m-m'=0$ or $m-m'=\pm 4$. Furthermore, the time-inversion symmetry, preserved in the absence of spin-orbit coupling, results in the equivalence of the elements with opposite sign of the m quantum number. Finally, the fourfold axis perpendicular to the quantization axis is responsible for the remaining dependence of the nonzero elements. The two independent matrix elements correspond to the two irreducible representations of the cubic group in d subspace. Using expressions for the e_g and t_{2g} representations in terms of spherical harmonics, it can directly be

TABLE I. Diagonal elements of the d density matrix for the (001) and (111) quantization axes, that correspond to the partial densities of states.

$ m $	(001)	(111)
0	B	A
1	A	$\frac{A+2B}{3}$
2	$\frac{A+B}{2}$	$\frac{2A+B}{3}$

TABLE II. Relative transition probabilities $a_{\gamma s}^+$ and $a_{\gamma s}^0$ at the L_2 edge ($j=1/2$).

γ	$a_{\gamma s}^+$		$a_{\gamma s}^0$	
	\uparrow	\downarrow	\uparrow	\downarrow
-1	2	3	6	4
1	3	12	4	6

shown that B is the density of states with e_g symmetry per state (i.e., $2B$ is the total e_g density of states) and A is the density of states with t_{2g} symmetry per state (i.e., $3A$ is the total t_{2g} density of states).

Upon a change of the quantization axis the density matrix transforms according to $D' = U^+ D U$, where U is a unitary representation of the transformation from the old to the new quantization axis in the d subspace. This transformation is not unique (any rotation along the quantization axis can be added), but as far as we are concerned only with the diagonal elements in formula (3) does the arbitrariness not play a role. The diagonal elements of the density matrix expressed in terms of A and B are shown in Table I for the (001) and (111) quantization axes.

TABLE III. Relative transition probabilities $a_{\gamma s}^+$ and $a_{\gamma s}^0$ at the L_3 edge ($j=3/2$).

γ	$a_{\gamma s}^+$		$a_{\gamma s}^0$	
	\uparrow	\downarrow	\uparrow	\downarrow
-3	0	3	0	9
-1	1	6	3	8
1	6	6	8	3
3	18	0	9	0

APPENDIX B: $a_{\gamma s}^\mu$ TABLES

Here we list the numerical values of the $a_{\gamma s}^\mu(j)$ coefficients for $j=1/2$ and $j=3/2$. As the $a_{\gamma s}^+$ and $a_{\gamma s}^-$ coefficients are related by

$$a_{\gamma s}^+(j) = a_{-\gamma-s}^-(j), \quad (\text{B1})$$

we present in the following Tables II and III only one of them. Since we deal only with relative quantities, the $a_{\gamma s}^\mu$ coefficients given in the tables have been rescaled with a constant prefactor to make them integer values for sake of simplicity.

*Electronic address: kunes@fzu.cz

¹C.T. Chen, Y.U. Idzerda, H.-J. Lin, N.V. Smith, G. Meigs, E. Chaban, G.H. Ho, E. Pellegrin, and F. Sette, Phys. Rev. Lett. **75**, 152 (1995).

²D. Weller, J. Stöhr, A. Carl, M.G. Samant, C. Chappert, R. Mégy, P. Beauvillain, P. Veillet, and G.A. Held, Phys. Rev. Lett. **75**, 3752 (1995).

³N. Nakajima, T. Koide, T. Shidara, H. Miyauchi, H. Fukutani, A. Fujimori, K. Iio, T. Katayama, M. Nývlt, and Y. Suzuki, Phys. Rev. Lett. **81**, 5229 (1998).

⁴P. Gambardella, A. Dallmeyer, K. Malt, M.C. Malagoli, W. Eberhardt, K. Kern, and C. Carbone, Nature (London) **416**, 301 (2002).

⁵J.B. Kortright and S.-K. Kim, Phys. Rev. B **62**, 12 216 (2000).

⁶H.-Ch. Mertins, P.M. Oppeneer, J. Kuneš, A. Gaupp, D. Abramsohn, and F. Schäfers, Phys. Rev. Lett. **87**, 047401 (2001).

⁷M.M. Schwickert, G.Y. Guo, M.A. Tomaz, W.L. O'Brien, and G.R. Harp, Phys. Rev. B **58**, R4289 (1998).

⁸S.S. Dhesi, G. van der Laan, E. Dudzik, and A.B. Shick, Phys. Rev. Lett. **87**, 067201 (2001).

⁹P. Kuiper, B.G. Searle, P. Rudolf, L.H. Tjeng, and C.T. Chen, Phys. Rev. Lett. **70**, 1549 (1993).

¹⁰W. Zhu, L. Seve, R. Sears, B. Sinkovic, and S.S.P. Parkin, Phys. Rev. Lett. **86**, 5389 (2001).

¹¹W.J. Antel, F. Perjeru, and G.R. Harp, Phys. Rev. Lett. **83**, 1439 (1999).

¹²S. Gota, M. Gautier-Soyer, and M. Sacchi, Phys. Rev. B **64**, 224407 (2001).

¹³G.Y. Guo, H. Ebert, W.M. Temmerman, and P.J. Durham, Phys. Rev. B **50**, 3861 (1994); G.Y. Guo, H. Ebert, W.M. Temmerman, and P.J. Durham, in *Metallic Alloys: Experimental and Theoretical Perspectives*, edited by J.S. Faulkner and R.G. Jordan (Kluwer, Dordrecht, 1994), pp. 339–348.

¹⁴G. van der Laan, Phys. Rev. Lett. **82**, 640 (1999).

¹⁵P.M. Oppeneer, in *Handbook of Magnetic Materials*, edited by K.H.J. Buschow (Elsevier, Amsterdam, 2001), Vol. 13, pp. 229–422.

¹⁶D.P. Siddons, M. Hart, Y. Amemiya, and J.B. Hastings, Phys. Rev. Lett. **64**, 1967 (1990).

¹⁷J.B. Kortright, M. Rice, S.-K. Kim, C.C. Walton, and T. Warwick, J. Magn. Magn. Mater. **191**, 79 (1999).

¹⁸H.-Ch. Mertins, F. Schäfers, X. Le Cann, A. Gaupp, and W. Gudat, Phys. Rev. B **61**, R874 (2000).

¹⁹J. Kuneš, P.M. Oppeneer, H.-Ch. Mertins, F. Schäfers, A. Gaupp, W. Gudat, and P. Novák, J. Magn. Magn. Mater. **240**, 454 (2002).

²⁰H. Ebert, in *Spin-Orbit-Influenced Spectroscopies of Magnetic Solids*, edited by H. Ebert and G. Schütz (Springer, Berlin, 1996), pp. 159–177.

²¹J. Kuneš, P.M. Oppeneer, H.-Ch. Mertins, F. Schäfers, A. Gaupp, W. Gudat, and P. Novák, Phys. Rev. B **64**, 174417 (2001).

²²B. T. Thole, P. Carra, F. Sette, and G. van der Laan, Phys. Rev. Lett. **68**, 1943 (1992).

²³P. Carra, B.T. Thole, M. Altarelli, and X. Wang, Phys. Rev. Lett. **70**, 694 (1993).

²⁴R. Wu and A.J. Freeman, Phys. Rev. Lett. **73**, 1994 (1994).

²⁵P. Blaha, K. Schwarz, and J. Luitz, *WIEN'97, A Full Potential Linearized Augmented Plane Wave Package for Calculating Crystal Properties*, Karlheinz Schwarz, Technical University of Wien, Vienna, 1999, ISBN 3-9501031-0-4.

²⁶J. Kuneš, P. Novák, M. Diviš, and P.M. Oppeneer, Phys. Rev. B **63**, 20511 (2001).